Hierarchical Formation of Intrasplat Cracks in Thermal Spray Ceramic Coatings

Lin Chen, Guan-Jun Yang, Cheng-Xin Li, and Chang-Jiu Li

(Submitted January 31, 2016; in revised form April 19, 2016)

Intrasplat cracks, an essential feature of thermally sprayed ceramic coatings, play important roles in determining coating properties. However, final intrasplat crack patterns are always considered to be disordered and irregular, resulting from random cracking during splat cooling, since the detailed formation process of intrasplat cracks has scarcely been considered. In the present study, the primary formation mechanism for intrasplat cracking was explored based on both experimental observations and mechanical analysis. The results show that the intrasplat crack pattern in thermally sprayed ceramic splats presents a hierarchical structure with four sides and six neighbors, indicating that intrasplat crack patterns arise from successive domain divisions due to sequential cracking during splat cooling. The driving forces for intrasplat cracking are discussed, and the experimental data quantitatively agree well with theoretical results. This will provide insight for further coating structure designs and tailoring by tuning of intrasplat cracks.

1. Introduction

Thermal spraying is one of the most important approaches for depositing thermal barrier coatings, such as low-thermal-conductivity lanthanum zirconate (LZO) coating, for advanced gas turbines due to the low thermal conductivity resulting from a lamellar structure. Numerous intrasplat cracks and intersplat pores between lamellae are two essential features of thermally sprayed ceramic coatings (Ref 1, 2). In addition to the well-documented intersplat pores resulting from limited interlamellar bonding, intrasplat cracks also play an important role in determining coating properties, including thermal and mechanical properties. Although conventional coating structure models do not consider intrasplat cracks (Ref 3), their contribution to the thermal resistivity is estimated to be as high as 42-57% based on cutting of heat flow paths for a typical thermally sprayed ceramic coating (Ref 4). The much lower elastic modulus of coatings in the in-plane directions is also mainly attributed to intrasplat cracks (Ref 5). In addition, the elastic modulus of coatings in the out-of-plane direction is determined by the pore network composed of both intersplat pores and intrasplat cracks (Ref 5). Therefore, study of the crack formation

mechanism and cracking control approaches is essentially to meet the requirements of different coating applications.

Although intrasplat cracks can be widely found in many publications, in-depth understanding of the intrasplat crack formation mechanism is not yet available. To date, it is well known that the presence of intrasplat cracks is usually due to stress relaxation during rapid cooling of ceramic splats (Ref 6-9). Kuroda and Clyne proposed a simple equation to estimate the tensile stress of splats during cooling after splat solidification (Ref 6), demonstrating that intrasplat cracks would inevitably occur in ceramic coatings as the stress is much larger than the material tensile strength. As a consequence, individual splats are divided into many small segments (or cells) by intrasplat cracks. Since thermally sprayed coatings are successively deposited by individual splats, intrasplat cracks in individual splats have been recognized to occur independently and uniformly, then intersecting with each other to form a complex network (Ref 1, 10).

Qualitatively, the final crack pattern is often considered as a disordered pattern, since the segments are often regarded as exhibiting an irregular morphology due to the random appearance of intrasplat cracks (Ref 1, 10-12). Intrasplat crack morphologies might also be influenced by crack paths (either inter- or transgranular); for example, some reports in literature argue that intrasplat crack resistance may be improved by inter- rather than transgranular cracking (Ref 13, 14). However, most cracks present a zigzag morphology, indicating that intrasplat cracking is generally intergranular. In summary, the essential formation mechanism of intrasplat cracks is not well understood due to the complexity of this phenomenon, seeming to be random.

Quantitatively, the intrasplat crack density, determined by the segment size, in individual splats can be analyzed statistically (Ref 1, 9, 15, 16). The mean segment size is reported to increase with increasing deposition tempera-

Lin Chen, Guan-Jun Yang, Cheng-Xin Li, and **Chang-Jiu Li**, State Key Laboratory for Mechanical Behavior of Materials, School of Materials Science and Engineering, Xi'an Jiaotong University, Xi'an 710049, Shaanxi, People's Republic of China. Contact e-mail: ygj@mail.xjtu.edu.cn.

ture (Ref 15). However, there is little information on how to tailor the segment size. Where and how intrasplat cracks initiate and propagate is also scarcely reported, since quantitative descriptions, except for some very simple measurements, of intrasplat cracks have been nearly impossible to date.

As a consequence of intrasplat cracking, the residual stress in the coating can be significantly decreased. Compared with the very large tensile stress in splats, which can reach as high as several GPa, the residual stress in plasma-sprayed coatings is usually on the order of ~100 MPa (Ref 17-19). However, the fraction and degree of stress relief offered by intrasplat cracking during deposition have rarely been characterized, since detailed understanding of the initiation and propagation of intrasplat cracks has not been available to date (Ref 20).

In this study, the primary formation mechanism for intrasplat cracking was explored based on both experimental observations and mechanical analysis. Such understanding of intrasplat cracking will allow correlation with the actual behavior of thermal spray coatings, thereby providing insight for further coating structure designs and tailoring by tuning intrasplat cracks.

2. Experiment

2.1 Materials

A thermally sprayed coating is built up from successive impingements of molten droplets, so understanding the microstructure of a single splat can provide rational understanding of the underlying fundamental mechanism. In this study, lanthanum zirconate (LZO), as a candidate material for next-generation thermal barrier coatings with low thermal conductivity and high-temperature phase stability, was used as a model material. As shown in Fig. 1(a), the LZO agglomerate powder used had particle size ranging from 5 to 25 μm with mean of 17.8 μm. In addition, $La_{0.5}Sr_{0.5}CoO_3$ (LSCO) and titania (TiO_2) were also used for comparison. The agglomerate LSCO powder (Fig. 1b) and fused-crushed TiO_2 (Fig. 1c) powder had larger particle size of 30–50 μm. To avoid any influence from the substrate surface profile and grain boundaries exposed on the substrate surface, the LZO, TiO_2, and LSCO splats were deposited on single-crystal Al_2O_3, TiO_2, and Si substrates with well-polished surface finish, respectively. The single-crystal substrates were square with side length of 10 mm and thickness of 500 μm out of the plane.

2.2 Splat Deposition

A commercial plasma spray system (GP-80, Jiujiang, China) was used to deposit splats at plasma arc power of 44 kW and spray distance of 80 mm. An external powder feeding injector was employed. Figure 2 shows a schematic diagram of the experimental setup for splat deposition. To avoid splat splashing, which hampers splat observation, the substrate was preheated to 500 °C using a
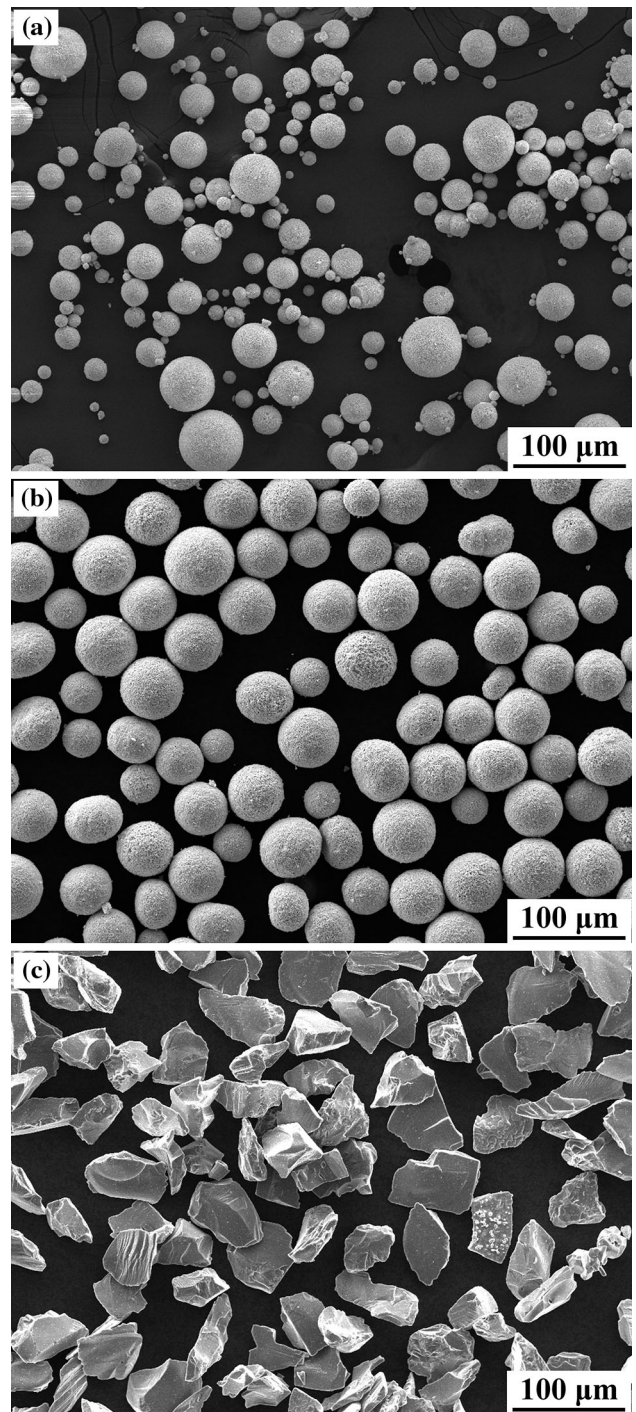

Fig. 1 Surface morphologies of agglomerate LZO powder (a), agglomerate LSCO powder (b), and fused-crushed TiO_2 powder (c)

copper plate heater below the substrate. The substrate surface temperature was monitored using a calibrated thermocouple. In addition, to avoid heating of the substrate by the plasma arc, a shielding plate was placed over the substrate. After splat deposition, the splat together with the substrate was cooled down to room temperature in atmosphere.
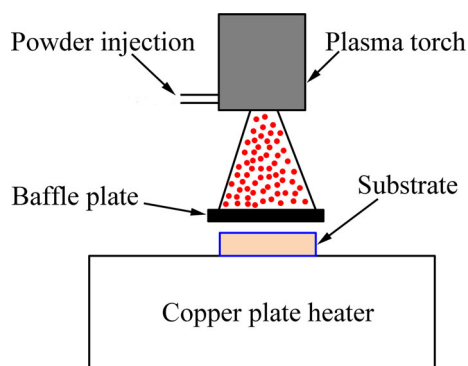
Fig. 2 Schematic of splat spray device

2.3 Characterization of Coatings

The surface morphologies of splats were examined using scanning electron microscopy (SEM, VEGA II-XMU, TESCAN, Czech Republic). The crystal orientation of splats was examined by the electron backscattered diffraction (EBSD, AZtec, Oxford Instruments, UK) method. The size of fragments divided by intrasplat cracks was determined using ImageJ software on SEM images obtained at magnification of 5000× or 10,000×. ImageJ software is widely applied for image processing; the image resolution in the present study was 1024×968 pixels with measurement accuracy of about 0.1 μm. To visualize the polycrystalline structure of the LZO splats, atomic force microscopy (AFM, Bruker, Germany) was used to examine the surface profile.

3. Results

3.1 Intrasplat Crack Morphology

Figure 3 shows the overall surface morphology of a single LZO splat deposited on a single-crystal Al_2O_3 substrate. It presents a typical segmented surface morphology divided by intrasplat cracks. This morphology can be found for nearly all kinds of thermally sprayed ceramic splats. The crack pattern shown in Fig. 3(a) seems disordered and irregular due to the zigzag crack paths. From the higher-magnification image shown in Fig. 3(b), it can be found that the crack width is distributed over a wide range. All the intrasplat cracks seem to be divided into different groups, for example, some wider cracks (marked by thick arrows) with longer interspacing and some narrower cracks (marked by thin arrows) with shorter interspacing. At the much higher magnification in Fig. 3(c), it can be found that the cracks proceeded along zigzag paths resulting from cracking along columnar grain boundaries in the splat, as shown in Fig. 3(d).

To further probe the formation mechanism of intrasplat cracks by eliminating the possible influence of grain boundary in the splat, single-crystalline splats of TiO_2 were deposited and observed, as shown in Fig. 4. In this study, TiO_2 splats were deposited on rutile TiO_2 sin-

gle-crystal substrate with out-of-plane direction [100] and [001]. The splats shown in Fig. 4(a) and (c) were deposited on the substrates with out-of-plane direction [100] and [001], respectively. Figure 4(b) shows a typical orientation map of the splat shown in Fig. 4(a) as obtained by EBSD, clearly suggesting that a single-crystalline TiO_2 splat is indeed formed during deposition. Both the single-crystal splats shown in Fig. 4(a) and (c) present very regular cubic segmented morphology resulting from regular intrasplat cracks. Moreover, the crack width and spacing (Fig. 4d) are similar to those of the LZO splat cracks (Fig. 3b). Some wider cracks (marked by thick arrows) have longer interspacing, while some narrower cracks (marked by thin arrows) have shorter interspacing. It is well known that single-crystalline splats of rutile-type TiO_2 have tetragonal structure with in-plane symmetry ($a = b \neq c$). For simplicity, all the TiO_2 splats mentioned below were deposited on substrates with out-of-plane direction [001]. It was also found that the cracks tended to intersect the substrate edge (with direction of $\langle 100 \rangle$) at angles of about 45°; namely, cracks were often orientated in the direction of $\langle 110 \rangle$.

Comparing the polycrystalline LZO splats with the single-crystal TiO_2 splats, the difference lies mainly in the presence or absence of grain boundaries. To further probe the influence of grain boundary on the crack pattern, LSCO, a nearly in-plane isotropic crystalline material, was deposited on Si wafer with a thin oxide surface. The crack patterns of LSCO splats shown in Fig. 5 seem different from those of both LZO polycrystalline splats and TiO_2 single-crystal splats. It has been reported that perovskite-type materials, such as LSCO, can easily lose oxygen during splat deposition, resulting in large lattice distortions (Ref 21-23). Orientation maps and Kikuchi patterns could not be obtained for LSCO splats by EBSD, suggesting that amorphous LSCO splats probably formed due to rapid cooling. This is consistent with the fact that the LSCO splats present an extraordinarily smooth surface without distinguishable grains at high magnification (50,000×), as shown in Fig. 5(b), suggesting superior in-plane isotropy of the LSCO splats. The cracks in the LSCO splats were similar to those in the TiO_2 splats but slightly curved, and the segments resulting from the cracks were irregular, being similar to the LZO splats.

3.2 Statistical Description of Fragments Divided by Crack Pattern

Analysis of crack and fragment morphologies appears to be a geometrical problem. However, the detailed formation mechanisms of fragments also need to be based on topology theory. To comprehensively identify regularities in the splat fragments, both clear connections and differences between geometry and topology must be stated. A clear distinction between topology and geometry is stated here based on Fig. 6. According to topology theory, edges and vertices are applied to describe the space-dividing network. A vertex in topology is a point where a younger crack meets an older one, and an edge is a part of a crack between two adjacent vertices (Ref 24, 25). By contrast,
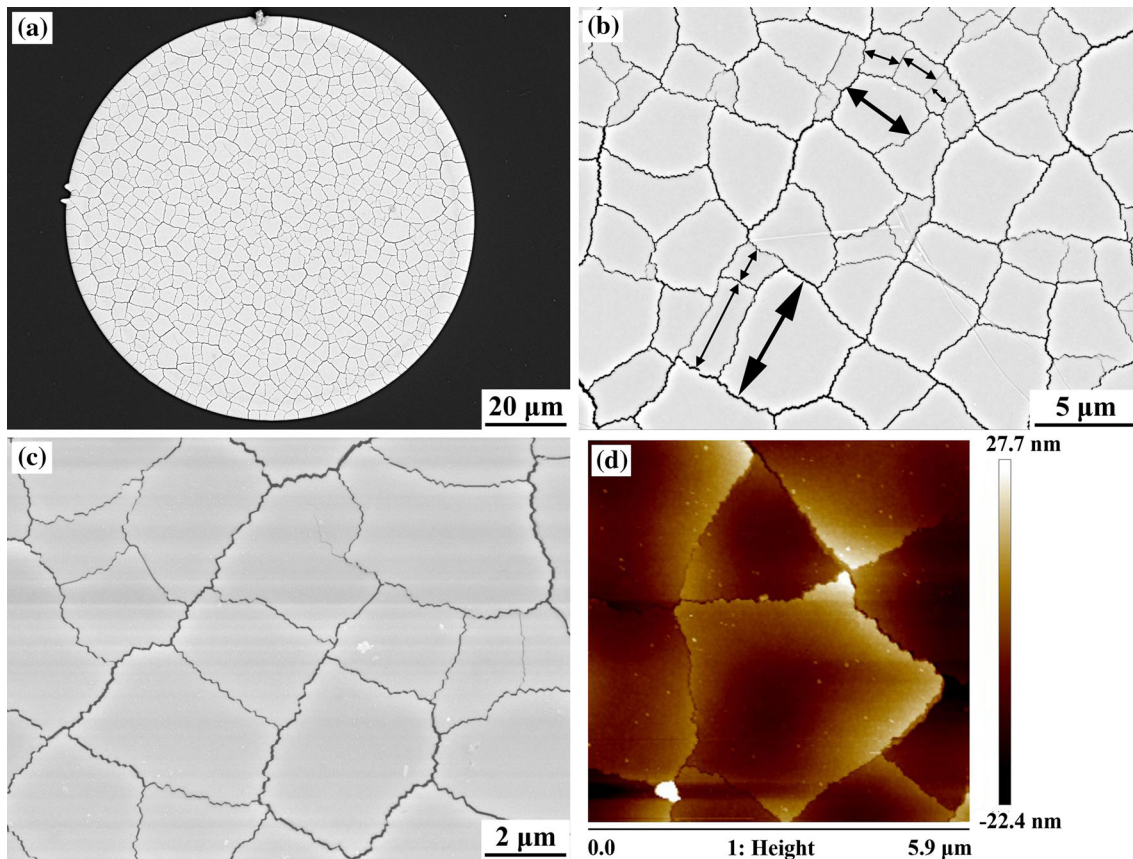
Fig. 3 Crack morphologies of polycrystalline LZO splats deposited on single-crystal Al_2O_3 substrate at 500 °C. The overall surface morphology of a single LZO splat is shown in (a). The widely ranging crack width and spacing are shown in (b) with some examples marked by thick and thin arrows. The zigzag crack paths are shown in (c) at high magnification, while the columnar grain boundaries and intergranular cracking are also clearly shown in the atomic force microscopy (AFM) image (d)

according to geometry theory, "sides" and "wedges" (or "corners") have to be considered to describe the shape of a cell. A side of a pattern is a part of the contour delimited by two wedge-shaped singularities (corners) (Ref 24, 25). Moreover, a side can be curved, but its curvature ought to be continuous in geometry. Consequently, the points where two edges intersect in a specified pattern correspond to vertices in topology but do not necessarily form wedges in geometry; for example, the cell marked with a black dot at the center in Fig. 6(a) has six vertices and six edges in topology, while it has four wedges and four sides in geometry. For LZO splats, due to their zigzag crack paths, a side is additionally defined as a contour consisting of several edges belonging to the same parent crack (as shown in Fig. 6b). The cell marked with a red dot at the center in Fig. 6(b) also has six vertices and six edges in topology, while it has four wedges and four sides in geometry. It is clear that, in each pattern, the number of corners is equal to the number of sides in geometry, and the number of vertices is equal to the number of edges in topology. In addition, the number of neighbors in each cell is equal to the number of edges in topology. However, the number of edges per cell is not necessarily equal to the number of sides. Using this approach, the number of both sides and neighbors in crack patterns were analyzed sta-

tistically for TiO_2, LSCO, and LZO splats. Figure 7 shows statistical histograms of the number of sides (black bars) and neighbors (red bars) for $N = 1000$ patterns in TiO_2, LSCO, and LZO splat segments. As presented in Table 1, the average number of sides for TiO_2, LSCO, and LZO splat segments was 4.0, 4.0, and 4.4, respectively. The average number of neighbors for TiO_2, LSCO, and LZO splat segments was 5.9, 5.9, and 5.7, respectively. These statistical results yield that the average number of sides and neighbors is roughly 4 and 6, respectively.

4. Discussion

4.1 Sequential Intrasplat Cracking

It is obvious that intrasplat cracks arise from fracture during cooling of splats. Many factors influence cracking behavior. The two most essential factors are cracking motivation (stress condition) and cracking resistance. Where cracking initiates and propagates generally depends on the maximum ratio between cracking motivation and resistance (Ref 26), i.e., either greatest motivation or least resistance. Therefore, the cracking behavior of a splat during cooling can be analyzed by mechanical anal-
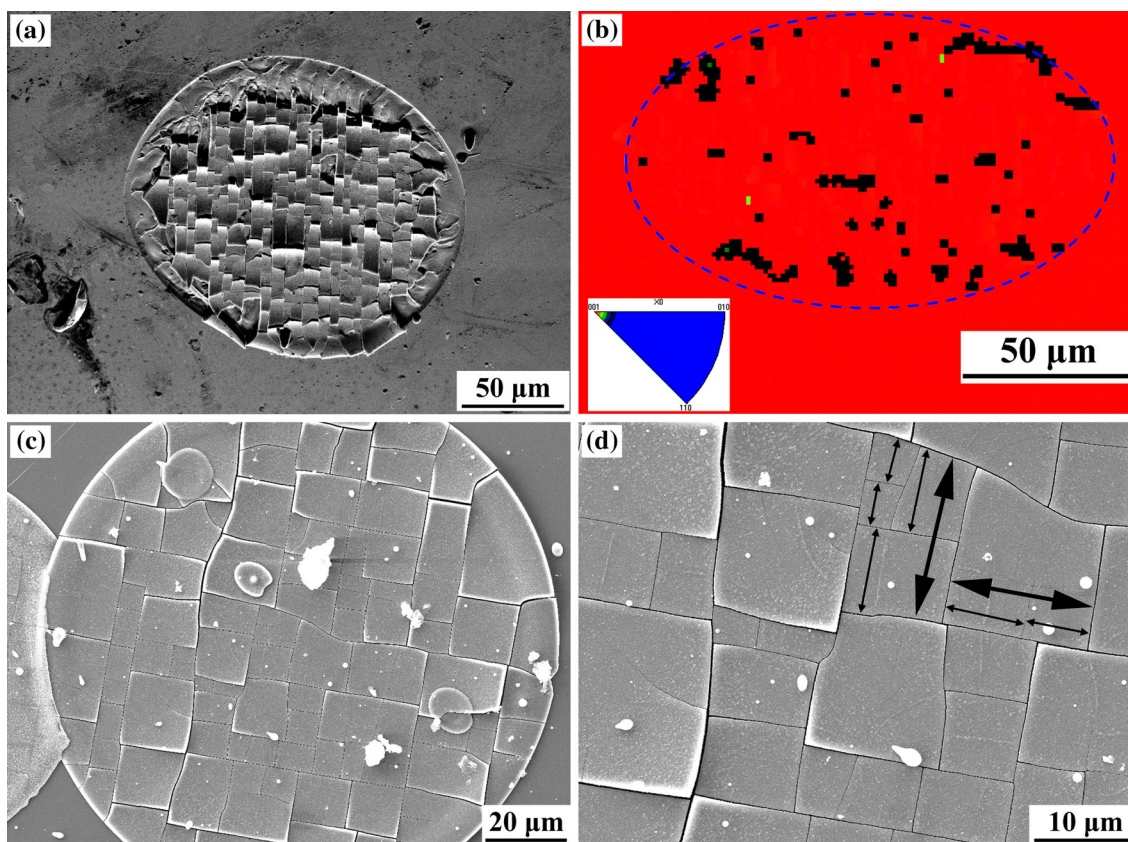
Fig. 4 Crack morphologies of single-crystal TiO$_2$ splats deposited on single-crystal rutile TiO$_2$ substrate at 500 °C. (a) Splat on substrate with out-of-plane direction [100]. (b) Orientation map of splat shown in (a) by EBSD, indicating a single-crystalline TiO$_2$ splat. (c) Splat on substrate with out-of-plane direction [001]. (d) Wide-ranging crack width and spacing, with some examples marked by thick and thin arrows. The splat shape (marked by ellipse with blue dashed line) shown in (b) became elliptical due to image shift during EBSD examination (Color figure online)

ysis. However, the sources of stress in a thermally sprayed splat are complicated, since stress may result from cooling-induced shrinkage (intrinsic stress) (Ref 6, 27, 28), thermal expansion mismatch between the splat and deposition substrate (thermal stress) (Ref 29, 30), and phase transformation-induced volume change (Ref 31, 32). For the three types of splats in this study, there is no phase transformation-induced volume change. Therefore, the stress in the splat only consists of intrinsic stress and thermal stress. The most typical characteristic of intrinsic and thermal stresses is that both are time dependent and increase sequentially with temperature. The theoretical total shrinkage strain from the melting temperature (T_m) to room temperature for conventional thermal spray is estimated to be roughly $\alpha \cdot T_m$. An empirical relationship between the melting temperature (T_m) and the coefficient of thermal expansion (CTE) is as follows (Ref 33):

$$\alpha \cdot T_m \approx 0.02. \tag{Eq 1}$$

In fact, the splat starts to solidify at a temperature several hundred degrees below the melting temperature (T_m) due to supercooling, and the substrate is often preheated to several hundred degrees to avoid splat splashing. Both of these effects contribute to decrease the theoretical

shrinkage strain. Consequently, a conservative estimate is assumed herein, i.e., half of the above-mentioned value of 0.02, i.e., 1% (for detailed analysis see Eq 9 in "Hierarchical Structure for TiO$_2$ and LSCO Splats" section). It is known that ceramic material generally has strength on the order of several hundred MPa, while the modulus is on the order of several hundred GPa. Compared with the strength on the order of several hundred MPa, the intrinsic stress can reach as high as several GPa, corresponding to a conservative estimate of the shrinkage strain. Therefore, it is reasonable to assume that, although inaccurate and qualitative, cracking must begin at an intermediate time during the cooling process. Consequently, intrasplat cracking is a successive rather than simultaneous process, which may well be the reason why cracks have different widths with alternate arrangement.

4.2 Successive Domain Divisions

In the initial stages of splat cooling, the cracking motivation attains the greatest value everywhere except on the periphery. Therefore, cracking propagates preferentially along the direction of least resistance. However, in later stages, the crack patterns are dominated by the greatest motivation, as the imperfections are exhausted
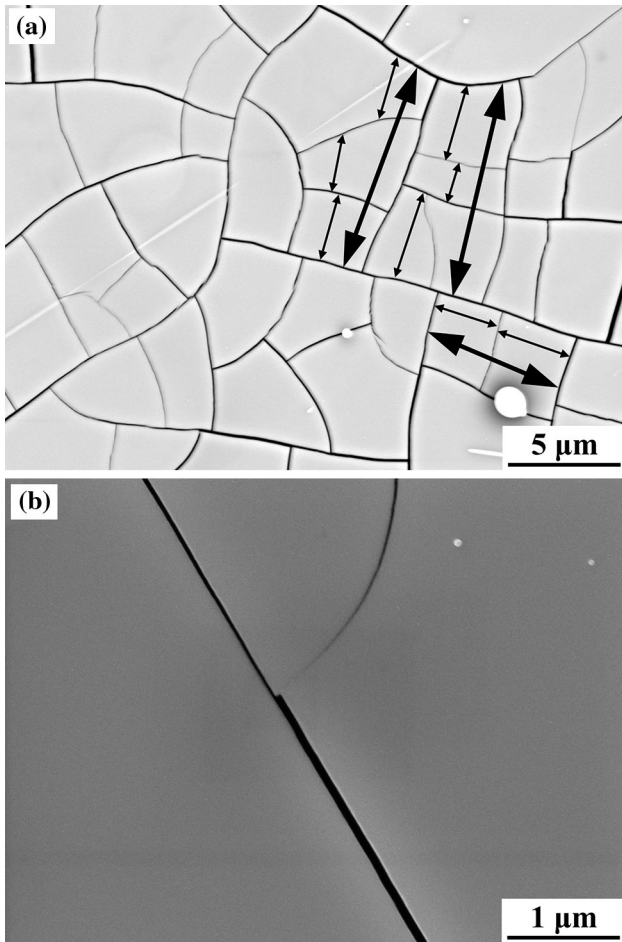
Fig. 5 Crack morphologies of polycrystalline LSCO splats deposited on Si wafer at 500 °C. The wide-ranging crack width and spacing are shown in (a) with some examples marked by thick and thin arrows. A straight and sharp crack located in an extraordinarily smooth surface is shown in (b) at high magnification, suggesting superior in-plane isotropy for LSCO splats

Fig. 6 Distinction between topology and geometry of LSCO patterns with straight crack paths (a) and LZO patterns with zigzag crack paths (b)

and the least resistance disappears. Intrasplat cracking (channeling process) is usually unstable. Once activated, it cannot arrest until it encounters another channel or an edge (Ref 26). Consequently, a connected crack network will emerge with sequential cracking. It is also well known that stress relief and redistribution occur as a result of cracking. To produce the maximal stress relief, cracks should propagate perpendicular to the direction along which the stress is greatest. The stress near an edge of a medium exists only in the direction parallel to it. Therefore, as cracking continues, a new crack near an older one should propagate perpendicular to it, and cracks should emerge and meet each other at right angles in patterns bounded by older cracks which are finally divided into smaller ones. As a result, the cracks for TiO_2 and LSCO splats are usually perpendicular to each other. Similar trends can also be found and analyzed for desiccation cracking (Ref 34-36).

Based on the analysis above, a detailed formation process for the intrasplat crack pattern can be outlined. In
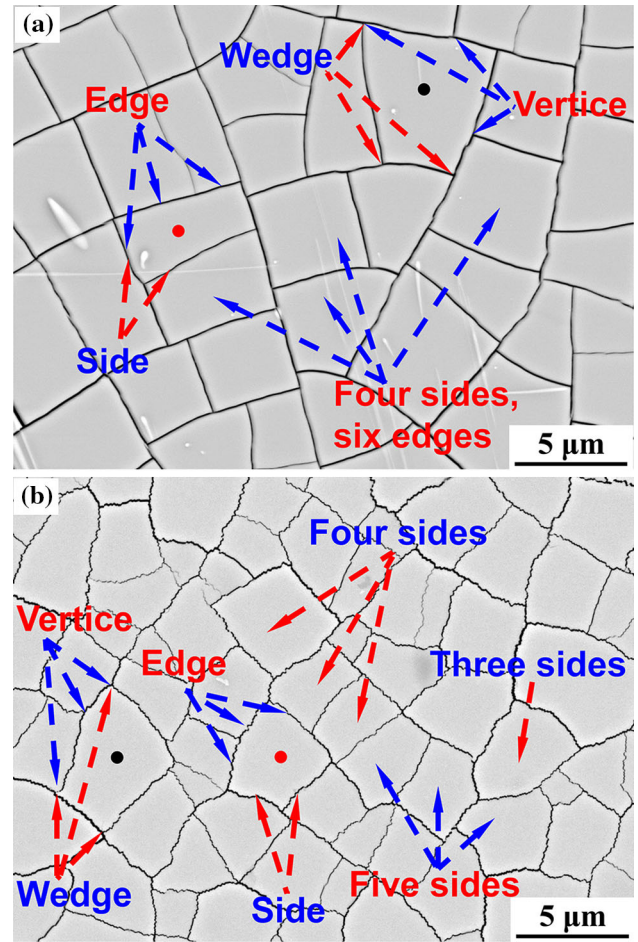
the initial stages, cracks propagate depending on the least resistance and divide the mother domain into several daughter domains. As the cracking process continues, cracks emerge in these daughter domains and divide each daughter domain into several next-generation domains of smaller size. Domain divisions proceed iteratively in this way and do not stop until the greatest motivation of the patterns is insufficient to drive further cracking. In the initial stages, several cracks can be generated simultaneously due to the sufficiently large domain size and limited stress relief by domain edges. However, as the domain divisions proceed iteratively, the size of the new-generation domains becomes so small that no more than one crack can propagate at a given time due to the sufficient stress relief and redistribution by domain edges. Finally, the new-generation domains are divided by bisection. It is obvious that each fracture divides one mother domain into two daughter domains, and the number of domains increases exponentially with each generation. Due to the independence of the domains, a fracture that joins a domain from the outside does not have any influence on the cell shape; the new crack clearly does not affect the
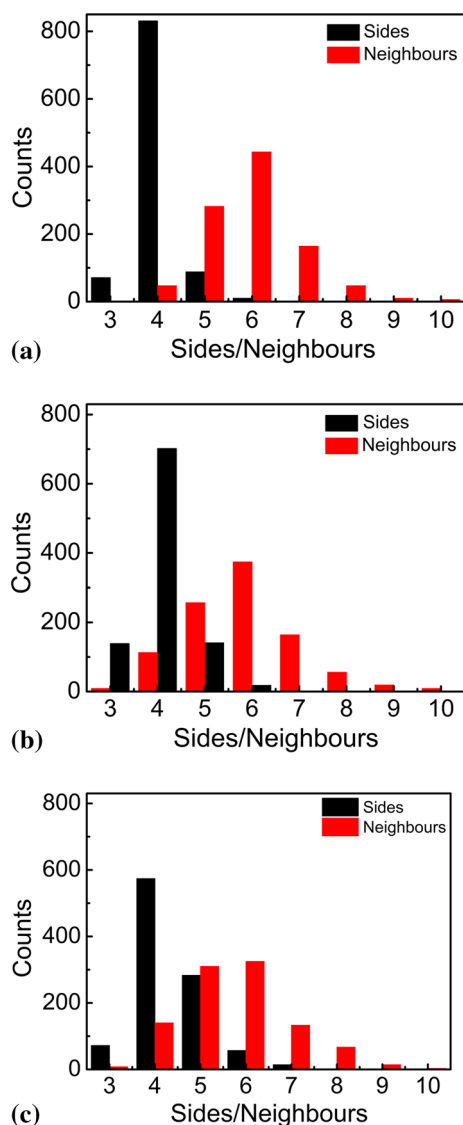
Fig. 7 Statistical histograms of the number of sides (black bars) and neighbors (red bars) for $N = 1000$ patterns in TiO_2 (a), LSCO (b), and LZO (c) splats (Color figure online)

Table 1 Average numbers of sides and neighbors

Splat	TiO_2	LSCO	LZO
Average number of sides	4.0	4.0	4.4
Average number of neighbors	5.9	5.9	5.7

position of the older ones. Although the initial crack and pattern morphologies seem slightly irregular, most of the final pattern morphologies present particular characteristics with successive domain divisions due to the limited domain effects and sequential cracking.

One should bear in mind that intrasplat cracking is a successive process, so crack patterns can be reconstructed by successive domain divisions based on the cracking criterion of the greatest motivation, as shown in Fig. 8. The

domain in Fig. 8(a) is selected to present the evolution of crack patterns from (b) to (f). As the crack driving force develops, a crack arises near the center, meeting the edges at 90°, as shown in Fig. 8(c). As the driving force continues to develop, cracking occurs successively and divides the domain into increasingly smaller patterns (d–f). With the decreasing domain size, the crack extension trajectory becomes increasingly deterministic. The domain divisions proceed iteratively in this way and do not stop until the greatest motivation of the patterns is insufficient to drive cracking. Finally, a particular hierarchy emerges.

4.3 Characteristics of Successive Cracking: Four Sides and Six Neighbors

It is clear that intrasplat crack patterns present hierarchical structures resulting from successive domain divisions due to sequential cracking, according to the qualitative analysis above. However, why the patterns exhibit hierarchical structures, on average, with four sides and six neighbors remains a question. In-depth understanding of the regularities of this hierarchy is therefore required. Such particular hierarchical structures with successive domain divisions are also widely found and explored in cracks observed in the glaze of ceramics and drying processes (Ref 24, 25, 37-40). In the case of soap froths and simultaneous cracking under biaxial stress, cellular patterns are usually formed as shown in Fig. 9(a), while hierarchical crack patterns will be generated for sequential cracking in a limited domain as shown in Fig. 9(b). These networks have a well-known common property expressed by Euler's theorem on topology, which states that, for a connected graph (network), the relation between the total number of vertices V, edges E, and separated cells N is given by (Ref 24, 37, 41)

$$N - E + V = O(1), \tag{Eq 2}$$

where $O(1)$ is a finite constant (generally equal to 2). It has been shown that, in a two-dimensional (2D) network, threefold vertices are most stable (Ref 24). Indeed, most vertices found in crack patterns of splats correspond to three edges. As a result, each vertex is shared by three cells, while each edge is shared by two cells. One should bear in mind that, in each pattern, the number of vertices (and neighbors) is equal to the number of edges, so the total numbers of edges and vertices in the whole network follow

$$3V = 2E \tag{Eq 3}$$

and the total number of neighbors Ψ is consequently

$$\Psi = 2E. \tag{Eq 4}$$

Combining Eq 2, 3, and 4, the average number of neighbors $\langle \psi \rangle$ becomes (Ref 24)

$$\langle \psi \rangle = \Psi/N = 6[1 - O(1)/N]. \tag{Eq 5}$$

In the case of an extended graph with large quantities of cells N, the average number of neighbors $\langle \psi \rangle$ per cell is thus equal to six. Indeed, the average number of neighbors
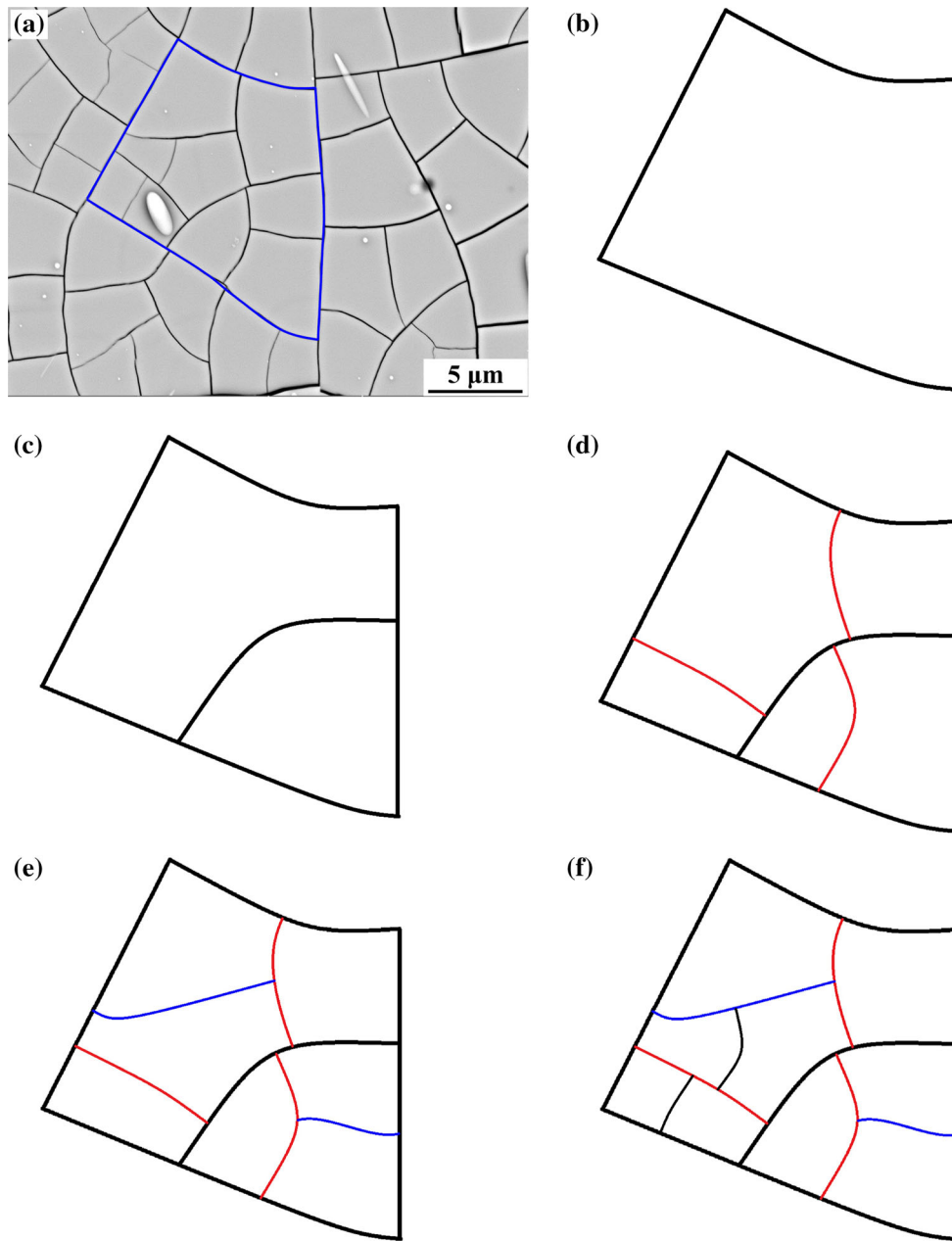
Fig. 8 Propagation from large to small scale. As the crack driving force develops, the crack patterns evolve from (b) to (f). Crack orders are shown from (c) to (f): first (bold black line), second (red lines), third (blue lines), and fourth (fine black lines) (Color figure online)

for the patterns in the TiO_2, LSCO, and LZO splats is roughly six.

In two-dimensional foams, as shown in Fig. 9(a), the angles at vertices are adjusted to 120°, being a signature of quasi-instantaneous force equilibrium at vertices in a topology (Ref 25). It is clear that each edge forms a side in each cell, and the number of sides in geometry is thus equal to the number of delimiting edges in topology. As a result, the average number of sides $\langle s \rangle$ per cell is also six, which is crucial for understanding two-dimensional soap froths (Ref 41, 42).

However, for a hierarchical structure with successive domain divisions, as shown in Fig. 9(b), a newer crack often propagates parallel to an older one and approaches another at a right angle to obtain the greatest motivation and stress relief. As a result, when a younger crack joins the contour of a cell from the outside at a right angle, it forms a vertex with a 180° angle (rather than 120° angle) inside the pattern because the older crack (the contour of the cell) has not been affected. Therefore, these vertices do not form wedges in the contour. The number of sides in geometry per cell is thus not equal to the number of
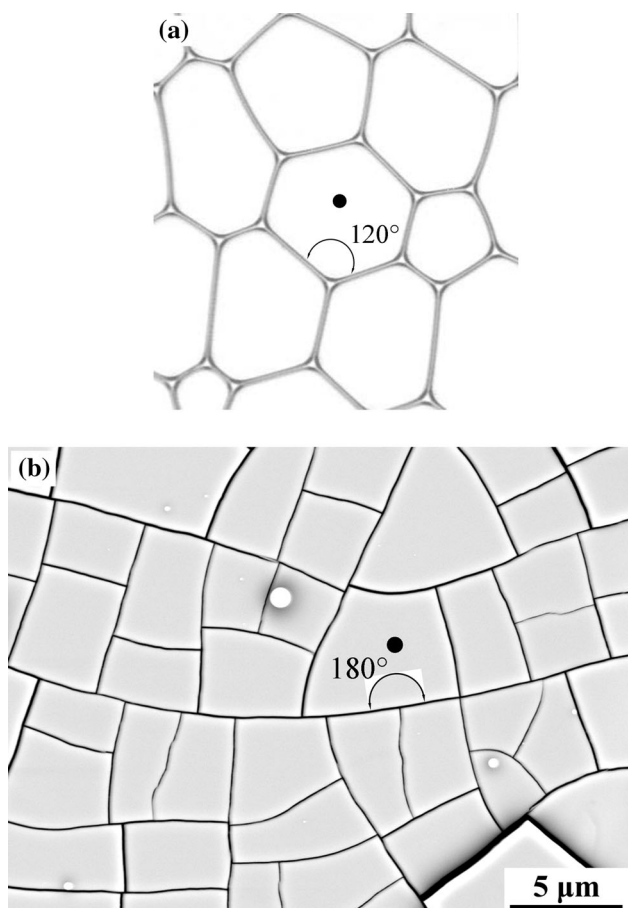
Fig. 9 Clear morphological differences between cellular structures and hierarchical structures. (a) Detail of a dry, two-dimensional foam (Ref 24). The cell marked by the disk has six sides and six neighbors, and the angle at the vertex is adjusted to 120°. (b) Detail of a hierarchical crack pattern of LSCO splats. The marked cell has four sides and six neighbors, and the angle at the vertex inside the domain remains at 180° because the older crack has not been disturbed

neighbors in topology, being a direct result of the frozen hierarchy of the crack patterns (Ref 24). Since at each vertex one of the three angles is equal to 180°, namely each vertex is shared by three cells while each wedge is shared by only two cells based on the clear distinction between and definition of topology and geometry, the total number of wedges W becomes

$$W = 2V. \tag{Eq 6}$$

Combining Eqs 2, 3, and 6, the average number of wedges $\langle w \rangle$ in geometry per cell is

$$\langle w \rangle = W/N = 4[1 - O(1)/N]. \tag{Eq 7}$$

In the case of an extended pattern with large quantities of cells N, the average number of wedges $\langle w \rangle$ per cell is thus equal to four. As a result, each domain is, on average, four sided. Indeed, the average number of sides per cell for the TiO$_2$, LSCO, and LZO splats is roughly four.

In conclusion, the characteristic of four sides and six neighbors per cell is a direct result of and criterion for the frozen hierarchy of the crack patterns resulting from successive domain divisions through sequential cracking. This crack pattern for hierarchical space division is a meaningful model and is also observed in other systems, such as the cracks observed in the glaze of ceramics and drying processes (Ref 24, 25, 37-40), venation patterns of plant leaves (Ref 43), and even city street networks generated by human activity (Ref 24).

4.4 Hierarchical Structure for TiO$_2$ and LSCO splats

It is well known that intrasplat cracks initiate and propagate along either the greatest motivation or the least resistance (Ref 26). For single-crystal TiO$_2$ splats, the cleavage direction, i.e., $\langle 110 \rangle$ orientation, is usually the direction of least resistance for cracking. Indeed, the cracking direction of single-crystal TiO$_2$ splats is preferentially $\langle 110 \rangle$. It is obvious that the cleavage direction always exists everywhere. In the initial stages, when the cracking motivation is greatest everywhere except the periphery, cracking propagates along the cleavage direction, developing an extraordinarily regular morphology. In later stages, since the cracking motivation is greatest only in a limited zone with successive division of the regular domains, both the greatest motivation and the least resistance thus dominate. As a result, cracks are supposed to propagate along the cleavage direction (generally $\langle 110 \rangle$ orientation) in the specific zone of a domain center. The overall crack morphologies for TiO$_2$ splats thus present extraordinary regularities with hierarchical characteristics of four sides and six neighbors. It is clear that this theoretical analysis agrees well with the experimental results shown in Fig. 4 with cracks along $\langle 110 \rangle$ orientation and a crack pattern showing regular cubic morphology.

Compared with TiO$_2$ splats, LSCO splats present superior in-plane isotropy with nearly no defects, as shown in Fig. 5(b). The greatest motivation thus dominates throughout all the crack divisions. In the initial stages, cracks initiate and propagate randomly due to the greatest motivation being attained everywhere except the periphery. The cracks are thus slightly curved. It is obvious that the stress distribution completely depends on the domain boundaries for a finite domain. Cracks propagate nearly parallel to one boundary and perpendicular to the other. Some heredities of morphologies appear between new cracks and older ones. The overall crack morphologies for LSCO splats are thus slightly random but also exhibit hierarchical characteristics with four sides and six neighbors.

For a hierarchical crack structure, the crack patterns can be characterized by the square root of the pattern area (Ref 44-47). In this way, complex and reticular cracks can be considered equivalent to one-dimensional cracks with specific spacing. The square root of the pattern area for typical TiO$_2$ splats is termed the crack spacing, and its statistics are shown in Fig. 10. The minimum and maximum crack spacing is 4.54 and 16.41 μm, respectively, with
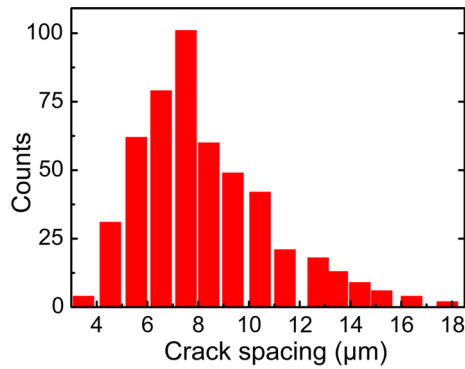
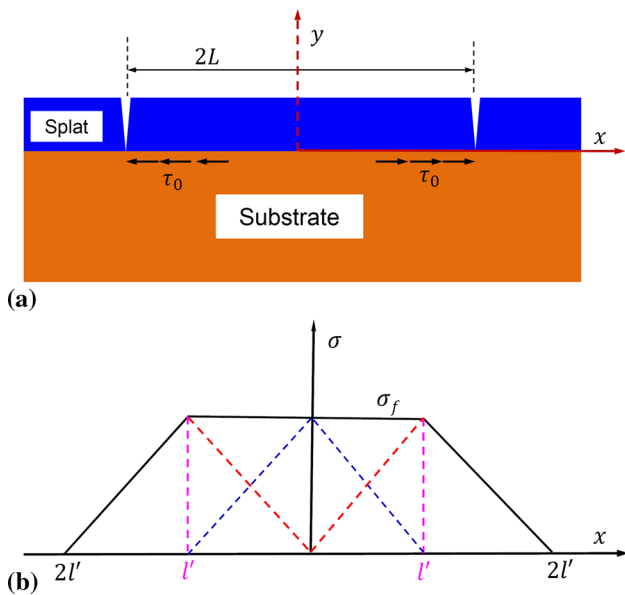**Fig. 10** Size distribution of TiO$_2$ fragments

Fig. 11 Schematic of shear-lag model for pattern size (a) and critical spacing distribution of newly formed crack between $2l'$ and $4l'$ (b)

mean of 8.27 μm. For film and substrate having identical elastic properties, the equilibrium crack spacing for sequential cracking is as follows (Ref 48):

$$\lambda_{\text{equilib}}/h \approx 5.6\sqrt{\Gamma_f/(E'\varepsilon^2 h)}, \tag{Eq 8}$$

where E' is given by $E' = E/(1 - v^2)$, Γ_f is the fracture surface energy, and h is the splat thickness. The elastic modulus E and Poisson ratio v for TiO$_2$ are about 205 GPa and 0.27, respectively. The thickness of a TiO$_2$ splat is about 1 μm. However, the shrinkage strain during deposition is unknown. The thermal strain from the deposition temperature (500 °C) to room temperature is nearly zero for the TiO$_2$/TiO$_2$ film/substrate system. Therefore, the intrinsic stress represents the major contribution to the cracking stress. The total shrinkage strain from the solid-

ification temperature (T_s) to the deposition temperature (T_D) is

$$\varepsilon_r \approx \alpha \cdot (T_s - T_D), \tag{Eq 9}$$

where T_s and T_D are about 1550 °C (considering 300 °C of supercooling) and 500 °C, respectively. The thermal expansion coefficient of TiO$_2$ is about $9 \times 10^{-6}/K$. The theoretical residual strain for TiO$_2$ splats is consequently about 0.94%.

It is worth bearing in mind that a fraction of the strain energy is relieved by other effects such as dislocations and stacking fault dislocations introduced prior to onset of cracking (Ref 49). It is appropriate to evaluate the strain energy by introducing a correction factor. Because the strain energy is related to the square of the strain, the equivalent residual strain can be expressed as

$$\varepsilon_e \approx \sqrt{1 - \beta} \cdot \alpha \cdot (T_s - T_D), \tag{Eq 10}$$

where the parameter β is a factor estimated to be about 0.2 when only considering 60° misfit dislocations in III–V epilayers grown on InP substrates (Ref 49). In the present study, considering the nonequilibrium nature of the splat deposition process due to the fast solidification and cooling, more defects probably exist in splats and β should consequently be larger (herein assumed to be 0.3). The theoretical residual strain for TiO$_2$ splats is thus about 0.79%.

Γ_f can be evaluated through the theory of Kelly (Ref 50, 51) as

$$\Gamma_f = \frac{Ea_0}{\pi^2}, \tag{Eq 11}$$

where a_0 is the relaxed interplanar spacing in the direction of the applied stress (direction of crack propagation). It is found that the cracks in TiO$_2$ splats were often orientated in the direction of $\langle 110 \rangle$, so a_0 is approximately equal to 0.325 nm. The crack surface energy Γ_f is thus evaluated to be about 6.66 J/m^2.

Combining Eq 8, 10, and 11, the equilibrium crack spacing is approximately equal to 4.16 μm. Our experimental value for the minimum crack spacing is about 4.54 μm, in quantitative agreement with this theoretical value.

However, the model mentioned above does not consider intersplat cracking. One can predict that the crack spacing will be significantly increased if intersplat cracking occurs. Shear-lag models have been extensively used and experimentally validated across a range of physical and natural systems. As shown in Fig. 11(a), supposing a constant shear stress at the interface in a finite zone, the tensile stress distribution in the splat is shown in Fig. 11(b) (Ref 52). The characteristic length l' can be calculated as follows:

$$l' = \frac{\sigma_f h}{\tau_0}. \tag{Eq 12}$$

If there is no transverse delamination in a fragment of size $2L$, the newly formed crack spacing must be between $2l'$ and $4l'$ with statistical mean of about $2.674l'$ (Ref 53). For
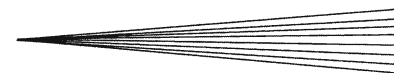
a large-scale TiO₂ splat, the supposed mean and maximum crack spacing is 6.07 and 9.08 μm, respectively, apparently different from the results shown in Fig. 10. It may be inappropriate to characterize the stress distribution using a simple shear-lag model, but the similar spacing trend is satisfactory. Transverse delamination occurs in fragments of size exceeding 9.08 μm.

4.5 Hierarchical Structure for LZO Splats

Looking at the crack patterns in the LZO splats, some factors must have deteriorated their hierarchical characteristics. The most likely factor is grain boundaries, as shown in Fig. 3(d). The cracking in the LZO splats is typically intergranular fracture and thus presents zigzag crack paths. It is well known that cracking propagates along either the greatest motivation or the least resistance (Ref 26). For LZO splats, due to the ubiquitous grain boundaries (defects), cracks nucleate readily, and the amount of nucleation is much greater than for TiO₂ or LSCO splats with limited defects. Cracks propagate along zigzag mainly through coalescence of independent nucleations. As a result, the networks present a disordered morphology. In the final stages of cracking, the patterns become so small that the greatest motivation is only located at the center of the domain. Cracking propagation thus strongly depends on the maximum ratio between the cracking motivation and resistance in this domain. A weak hierarchy arises in this way, becoming stronger with decreasing domain size.

5. Conclusions

The primary formation mechanism of LZO intrasplat cracking was explored and compared with TiO₂ and LSCO splats. The results show that TiO₂ single-crystal splats present a highly regular cubic segmented morphology resulting from regular intrasplat cracks, while the pattern for LZO and LSCO splats appears more irregular. However, all the intrasplat cracks present a wide range of crack width distribution, suggesting sequential rather than simultaneous cracking. To further understand the formation mechanism, the numbers of sides and neighbors of crack patterns were analyzed statistically based on topology and geometry theory. The results show that the intrasplat crack patterns for all three kinds of thermally sprayed ceramic splats present a hierarchical structure with four sides and six neighbors, indicating that all the intrasplat crack patterns arise through successive domain divisions due to sequential cracking during splat cooling. The driving forces for intrasplat cracking of TiO₂ splats are discussed in detail, and the statistical experimental data for crack spacing agree well quantitatively with the theoretical results. This will provide insight for further coating structure design and tailoring through tuning of intrasplat cracks.

References

1. A. Ohmori and C.J. Li, Quantitative Characterization of the Structure of Plasma-Sprayed Al₂O₃ Coating by Using Copper Electroplating, *Thin Solid Films*, 1991, **201**(2), p 241-252
2. R. Mcpherson, A Model for the Thermal-Conductivity of Plasma-Sprayed Ceramic Coatings, *Thin Solid Films*, 1984, **112**(1), p 89-95
3. I.O. Golosnoy, S.A. Tsipas, and T.W. Clyne, An Analytical Model for Simulation of Heat Flow in Plasma-Sprayed Thermal Barrier Coatings, *J. Therm. Spray Technol.*, 2005, **14**(2), p 205-214
4. H. Xie, Y.C. Xie, G.J. Yang, C.X. Li, and C.J. Li, Modeling Thermal Conductivity of Thermally Sprayed Coatings with Intrasplat Cracks, *J. Therm. Spray Technol.*, 2013, **22**(8), p 1328-1336
5. G.R. Li, B.W. Lv, G.J. Yang, W.X. Zhang, C.X. Li, and C.J. Li, Relationship Between Lamellar Structure and Elastic Modulus of Thermally Sprayed Thermal Barrier Coatings with Intra-splat Cracks, *J. Therm. Spray Technol.*, 2015, **24**(8), p 1355-1367
6. S. Kuroda and T.W. Clyne, The Quenching Stress in Thermally Sprayed Coatings, *Thin Solid Films*, 1991, **200**(1), p 49-66
7. N. Mifune and Y. Harada, Mechanism of Vertical Microcracking in CaO·SiO₂-CaO·ZrO₂ Sprayed Thermal Barrier Top Coating, *Mater. Trans.*, 2004, **45**(5), p 1788-1793
8. K. Ito, H. Kuriki, and M. Enoki, A Numerical Study on Generation Mechanism of Vertical Cracks in Top Coat of TBCs During APS Deposition, *J. Therm. Spray Technol.*, 2015, **24**(5), p 730-738
9. P. Bengtsson and C. Persson, Modelled and Measured Residual Stresses in Plasma Sprayed Thermal Barrier Coatings, *Surf. Coat. Technol.*, 1997, **92**(1-2), p 78-86
10. C.J. Li and A. Ohmori, Relationships Between the Microstructure and Properties of Thermally Sprayed Deposits, *J. Therm. Spray Technol.*, 2002, **11**(3), p 365-374
11. S. Rangarajan and A.H. King, Non-destructive Evaluation of Delamination in Ceramic Thin Films on Metal Substrates by Scanning Electron Microscopy, *Thin Solid Films*, 2001, **385**(1-2), p 22-28
12. T. Chraska and A.H. King, Effect of Different Substrate Conditions Upon Interface with Plasma Sprayed Zirconia—A TEM Study, *Surf. Coat. Technol.*, 2002, **157**(2-3), p 238-246
13. B. Liang and C.X. Ding, Thermal Shock Resistances of Nanostructured and Conventional Zirconia Coatings Deposited by Atmospheric Plasma Spraying, *Surf. Coat. Technol.*, 2005, **197**(2-3), p 185-192
14. D.Y. Chen, M. Gell, E.H. Jordan, E. Cao, and X.Q. Ma, Thermal Stability of Air Plasma Spray and Solution Precursor Plasma Spray Thermal Barrier Coatings, *J. Am. Ceram. Soc.*, 2007, **90**(10), p 3160-3166
15. Y.Z. Xing, Y. Li, C.J. Li, C.X. Li, and G.J. Yang, Influence of Substrate Temperature on Microcracks Formation in Plasma-Sprayed Yttria-Stabilized Zirconia Splats, *Key Eng. Mater.*, 2008, **373-374**, p 69-72
16. C.J. Li, G.J. Yang, and C.X. Li, Development of Particle Interface Bonding in Thermal Spray Coatings: A Review, *J. Therm. Spray Technol.*, 2013, **22**(2-3), p 192-206
17. J. Matejicek, S. Sampath, P.C. Brand, and H.J. Prask, Quenching, Thermal and Residual Stress in Plasma Sprayed Deposits: NiCrAlY and YSZ Coatings, *Acta Mater.*, 1999, **47**(2), p 607-617

18. J. Matejicek and S. Sampath, In Situ Measurement of Residual Stresses and Elastic Moduli in Thermal Sprayed Coatings—Part 1: Apparatus and Analysis, *Acta Mater.*, 2003, **51**(3), p 863-872

19. C.M. Weyant, K.T. Faber, J.D. Almer, and J.V. Guiheen, Residual Stress and Microstructural Evolution in Tantalum Oxide Coatings on Silicon Nitride, *J. Am. Ceram. Soc.*, 2005, **88**(8), p 2169-2176

20. J. Go, Y.G. Jung, S. Kim, and U. Paik, Analysis of Thermoelastic Characteristics for Vertical-Cracked Thermal Barrier Coatings Through Mathematical Approaches, *Surf. Coat. Technol.*, 2011, **206**(7), p 1615-1620

21. K. Huang, H.Y. Lee, and J.B. Goodenough, Sr- and Ni- Doped $LaCoO_3$ and $LaFeO_3$ Perovskites New Cathode Materials for Solid-Oxide Fuel Cells, *J. Electrochem. Soc.*, 1998, **145**(9), p 3220-3227

22. M. Gao, C.-J. Li, C.-X. Li, G.-J. Yang, and S.-Q. Fan, Microstructure, Oxygen Stoichiometry and Electrical Conductivity of Flame-Sprayed $Sm_{0.7}Sr_{0.3}CoO_{3-\delta}$, *J. Power Sources*, 2009, **191**(2), p 275-279

23. K.S. Anil, S.N. Nair, J. Alias, and S. Date, Evolution of the Cluster Glass System $La_{0.5}Sr_{0.5}CoO_3$, *J. Mater. Chem.*, 1998, **8**(10), p 2245-2251

24. S. Bohn, S. Douady, and Y. Couder, Four Sided Domains in Hierarchical Space Dividing Patterns, *Phys. Rev. Lett.*, 2005, **94**(5), p 054503

25. S. Bohn, Hierarchical Crack Patterns: A Comparison with Two-Dimensional Soap Foams, *Colloid Surf. A*, 2005, **263**(1-3), p 46-51

26. J.W. Hutchinson and Z. Suo, Mixed-Mode Cracking in Layered Materials, *Adv. Appl. Mech.*, 1992, **29**, p 63-191

27. S. Kuroda, T. Dendo, and S. Kitahara, Quenching Stress in Plasma-Sprayed Coatings and Its Correlation with the Deposit Microstructure, *J. Therm. Spray Technol.*, 1995, **4**(1), p 75-84

28. S. Kuroda, T. Fukushima, and S. Kitahara, Significance of Quenching Stress in the Cohesion and Adhesion of Thermally Sprayed Coatings, *J. Therm. Spray Technol.*, 1992, **1**(4), p 325-332

29. T.W. Clyne, Residual Stresses in Surface Coatings and Their Effects on Interfacial Debonding, *Interfacial Effects Part. Fibrous Layered Compos. Mater.*, 1996, **116-117**, p 307-330

30. T.W. Clyne and S.C. Gill, Residual Stresses in Thermal Spray Coatings and Their Effect on Interfacial Adhesion: A Review of Recent Work, *J. Therm. Spray Technol.*, 1996, **5**(4), p 401-418

31. P. Scardi, M. Leoni, and L. Bertamini, Influence of Phase Stability on the Residual Stress in Partially Stabilized Zirconia TBC Produced by Plasma Spray, *Surf. Coat. Technol.*, 1995, **76**(1-3), p 106-112

32. P.J. Withers and H.K.D.H. Bhadeshia, Overview—Residual Stress Part 2—Nature and Origins, *Mater. Sci. Technol.-Lond.*, 2001, **17**(4), p 366-375

33. P. Hidnert, and W. Souder, Thermal Expansion of Solids, NBS Circular, 1950, p 486

34. A. Groisman and E. Kaplan, An Experimental-Study of Cracking Induced by Desiccation, *Europhys. Lett.*, 1994, **25**(6), p 415-420

35. D. Mal, S. Sinha, T. Dutta, S. Mitra, and S. Tarafdar, Formation of Crack Patterns in Clay Films: Desiccation and Relaxation, *J. Phys. Soc. Jpn.*, 2007, **76**(1), p 014801

36. N. Lecocq and N. Vandewalle, Experimental Study of Cracking Induced by Desiccation in 1-Dimensional Systems, *Eur. Phys. J. E*, 2002, **8**(4), p 445-452

37. S. Bohn, L. Pauchard, and Y. Couder, Hierarchical Crack Pattern as Formed by Successive Domain Divisions. I. Temporal and Geometrical Hierarchy, *Phys. Rev. E*, 2005, **71**(4), p 046214

38. S. Bohn, J. Platkiewicz, B. Andreotti, M. Adda-Bedia, and Y. Couder, Hierarchical Crack Pattern as Formed by Successive Domain Divisions. II. From Disordered to Deterministic Behavior, *Phys. Rev. E*, 2005, **71**(4), p 046215

39. J. Richardi, A.T. Ngo, and M.P. Pileni, Simulations of Cracks Supported by Experiments: The Influence of the Film Height and Isotropy on the Geometry of Crack Patterns, *J. Phys. Chem. C*, 2010, **114**(41), p 17324-17332

40. K.A. Shorlin, J.R. de Bruyn, M. Graham, and S.W. Morris, Development and Geometry of Isotropic and Directional Shrinkage-Crack Patterns, *Phys. Rev. E*, 2000, **61**(6), p 6950-6957

41. J. Stavans, The Evolution of Cellular Structures, *Rep. Prog. Phys.*, 1993, **56**(6), p 733-789

42. D. Weaire and N. Rivier, Soap, Cells and Statistics - Random Patterns in Two Dimensions (Reprinted from Contemporary Physics, vol 25, page 59, 1984), *Contemp. Phys.*, 2009, **50**(1), p 199-239

43. Y. Couder, L. Pauchard, C. Allain, M. Adda-Bedia, and S. Douady, The Leaf Venation as Formed in a Tensorial Field, *Eur. Phys. J. B*, 2002, **28**(2), p 135-138

44. C.A. Tang, Y.B. Zhang, Z.Z. Liang, T. Xu, L.G. Tham, P.A. Lindqvist, S.Q. Kou, and H.Y. Liu, Fracture Spacing in Layered Materials and Pattern Transition from Parallel to Polygonal Fractures, *Phys. Rev. E*, 2006, **73**(5), p 056120

45. K. Leung and Z. Neda, Pattern Formation and Selection in Quasistatic Fracture, *Phys. Rev. Lett.*, 2000, **85**(3), p 662-665

46. K.T. Leung and Z. Neda, Criticality and Pattern Formation in Fracture by Residual Stresses, *Phys. Rev. E*, 2010, **82**(4), p 046118

47. S. Nag, S. Sinha, S. Sadhukhan, T. Dutta, and S. Tarafdar, Crack Patterns in Desiccating Clay-Polymer Mixtures with Varying Composition, *J. Phys. Condens. Mater.*, 2010, **22**(1), p 015402

48. M.D. Thouless, E. Olsson, and A. Gupta, Cracking of Brittle Films on Elastic Substrates, *Acta Metall. Mater.*, 1992, **40**(6), p 1287-1292

49. R.T. Murray, C.J. Kiely, and M. Hopkinson, Crack Formation in III-V Epilayers Grown Under Tensile Strain on InP(001) Substrates, *Philos. Mag. A*, 1996, **74**(2), p 383-393

50. R.T. Murray, C.J. Kiely, and M. Hopkinson, General Characteristics of Crack Arrays in Epilayers Grown Under Tensile Strain, *Semicond. Sci. Technol.*, 2000, **15**(4), p 325-33051

51. A. Kelly, *Strong Solids*, Oxford University Press, Oxford, 1966, p 3-11

52. A. Kelly and W.R. Tyson, Tensile Properties of Fibre-Reinforced Metals: Copper/Tungsten and Copper/Molybdenum, *J. Mech. Phys. Solids*, 1965, **13**(6), p 329-350

53. A.C. Kimber and J.G. Keer, On the Theoretical Average Crack Spacing in Brittle Matrix Composites Containing Continuous Aligned Fibers, *J. Mater. Sci. Lett.*, 1982, **1**(8), p 353-354